NEUROCHEMISTRY


10.1126/sciadv.1501672

# Dopamine $D_1$ signaling organizes network dynamics underlying working memory

Joshua L. Roffman,[1,2]* Alexandra S. Tanner,[1] Hamdi Eryilmaz,[1] Anais Rodriguez-Thompson,[1] Noah J. Silverstein,[1] New Fei Ho,[1] Adam Z. Nitenson,[1] Daniel B. Chonde,[2] Douglas N. Greve,[2] Anissa Abi-Dargham,[3] Randy L. Buckner,[1,2] Dara S. Manoach,[1,2] Bruce R. Rosen,[2] Jacob M. Hooker,[2] Ciprian Catana[2]

**Local prefrontal dopamine signaling supports working memory by tuning pyramidal neurons to task-relevant stimuli. Enabled by simultaneous positron emission tomography–magnetic resonance imaging (PET-MRI), we determined whether neuromodulatory effects of dopamine scale to the level of cortical networks and coordinate their interplay during working memory. Among network territories, mean cortical $D_1$ receptor densities differed substantially but were strongly interrelated, suggesting cross-network regulation. Indeed, mean cortical $D_1$ density predicted working memory–emergent decoupling of the frontoparietal and default networks, which respectively manage task-related and internal stimuli. In contrast, striatal $D_1$ predicted opposing effects within these two networks but no between-network effects. These findings specifically link cortical dopamine signaling to network crosstalk that redirects cognitive resources to working memory, echoing neuromodulatory effects of $D_1$ signaling on the level of cortical microcircuits.**

## INTRODUCTION

Performance of cognitive tasks requires reallocation of resources within and among cortical networks (*1*). Understanding the molecular mechanisms that govern such network dynamics is a longstanding goal of cognitive neuroscience. A well-studied example is the modulatory role of prefrontal dopamine signaling in working memory, a key component of executive function. Stimulation of prefrontal dopamine $D_1$ receptors facilitates working memory by potentiating responsiveness of pyramidal neurons to task-relevant stimuli and suppressing response to extraneous ones (*2*–*7*). These processes may contribute to activation of the dorsolateral prefrontal cortex (dlPFC), which is a key node in the frontoparietal control network (FPCN), during functional magnetic resonance imaging (fMRI) studies of working memory performance (*8*, *9*). Cortical (specifically, dlPFC) $D_1$ density (*10*) and dopamine release (*11*) have previously been related to activation in frontoparietal regions during working memory in sequential positron emission tomography (PET) and fMRI scans.

As with other cognitive tasks, working memory is also associated with deactivation of the default network (DN), which manages internal (and, hence, task-irrelevant) stimuli. Key DN nodes include medial prefrontal cortex (mPFC) and posterior cingulate cortex (pCing), which are regions that receive dense $D_1$ innervation through mesocorticolimbic projections (*12*), demonstrate robust coupling to the ventral tegmental area with resting-state fMRI (*13*), and exhibit enhanced deactivation following administration of a $D_1/D_2$ agonist (*14*).

Dopamine, thus, appears well positioned to modulate cortical networks that either dampen extraneous stimuli or amplify relevant ones, analogous to its roles in prefrontal microcircuits. Furthermore, indirect evidence suggests that dopamine may exert a unified, higher-order coordination of task-relevant and task-irrelevant networks. fMRI studies of catecholamine-releasing drugs (*15*), dopamine antagonists (*16*), and common polymorphisms in genes that regulate dopamine signaling (*17*, *18*) have implicated dopamine in the decoupling of FPCN and DN during working memory. However, mechanistic links between dopamine's modulatory effects on cellular physiology and working memory–associated network changes remain obscure. This partially reflects a longstanding technical limitation—that is, the inability to simultaneously measure indices of dopamine signaling and network function—but more fundamentally reflects a limited understanding of how dopaminergic projections map anatomically and functionally to cortical networks.

We used a novel PET-MRI platform (*19*) to study the distribution of cortical $D_1$ receptor binding potential (density) across network territories and to evaluate the relationship between $D_1$ signaling and functional connectivity (FC; coupling) of working memory–related networks.

## RESULTS

### Uncoupling of cortical networks during working memory

To define connectivity endpoints for the PET-MRI analysis, we first studied 100 healthy individuals using conventional fMRI. Immediately following a resting-state fMRI sequence, participants underwent task-based fMRI while performing a version of the Sternberg Item Recognition Paradigm (SIRP). Participants viewed one, three, five, or seven items (consonants) and then responded to a series of probes, indicating whether the presented letter was, or was not, a member of the memorized set (fig. S1 and table S1). Item load (that is, the number of memorized consonants) was linearly related to activation in dlPFC, intraparietal sulcus (iPS), anterior insula, and dorsal anterior cingulate (Fig. 1A). These regions overlap robustly and specifically with FPCN (Fig. 1B), as previously defined using resting-state fMRI data in 1000 non-overlapping individuals (*20*). Item load was also linearly related to deactivation in the mPFC, pCing, and inferior parietal lobule, which are regions that correspond to DN.

We then defined eight nodes within FPCN and DN around peak vertices of load-dependent activation or deactivation in the group map (table S2) for analyses of FC. Connectivity of between-network

[1]Department of Psychiatry, Massachusetts General Hospital, Harvard Medical School, 55 Fruit Street, Boston, MA 02114, USA. [2]Athinoula A. Martinos Center for Biomedical Imaging, Massachusetts General Hospital, 149 13th Street, Charlestown, MA 02129, USA. [3]Department of Psychiatry, Columbia University Medical Center, Harkness Pavilion, 180 Fort Washington Avenue, New York, NY 10032, USA.
*Corresponding author. Email: jroffman@partners.org

node pairs (that is, FPCN to DN) dropped precipitously as subjects moved from rest to task conditions and changed substantially more than the connectivity of within-network node pairs did (for example, FPCN to FPCN; condition × within-/between-network interaction, $P < 10^{-10}$) (Fig. 1, C and D). Although seeds for connectivity analysis were localized on the basis of the group map of task-related activation, the independence of these measures is indicated by the lack of meaningful correlation between local activation and connectivity ($-0.26 < R < 0.27$), either at rest or during the task (table S3).

### Distribution of $D_1$ receptors among cortical networks

A non-overlapping sample of 29 healthy individuals underwent simultaneous multimodal imaging with PET-MRI. The PET ligand was [$^{11}$C]NNC112, which has high selectivity for striatal $D_1$ receptors and has been associated with reliable cortical and subcortical signal in previous studies (*21*, *22*). When considering variability in NNC112 cortical signal across individuals, lower receptor density is usually interpreted as reflecting chronic exposure to higher synaptic dopamine concentrations (*23*). Because approximately 20 to 25% of cortical NNC112 signal represents binding to 5HT2a receptors (*24*), participants took 2 mg of oral risperidone 90 min before scanning, following previously published methods (*25*). Risperidone blocks 5HT2a receptors but has no affinity for $D_1$; accordingly, risperidone pretreatment markedly improves the specificity of cortical NNC112 signal for $D_1$.

PET data from two subjects were excluded because of early scan termination, leaving 27 subjects with usable PET data sets. As a measure of

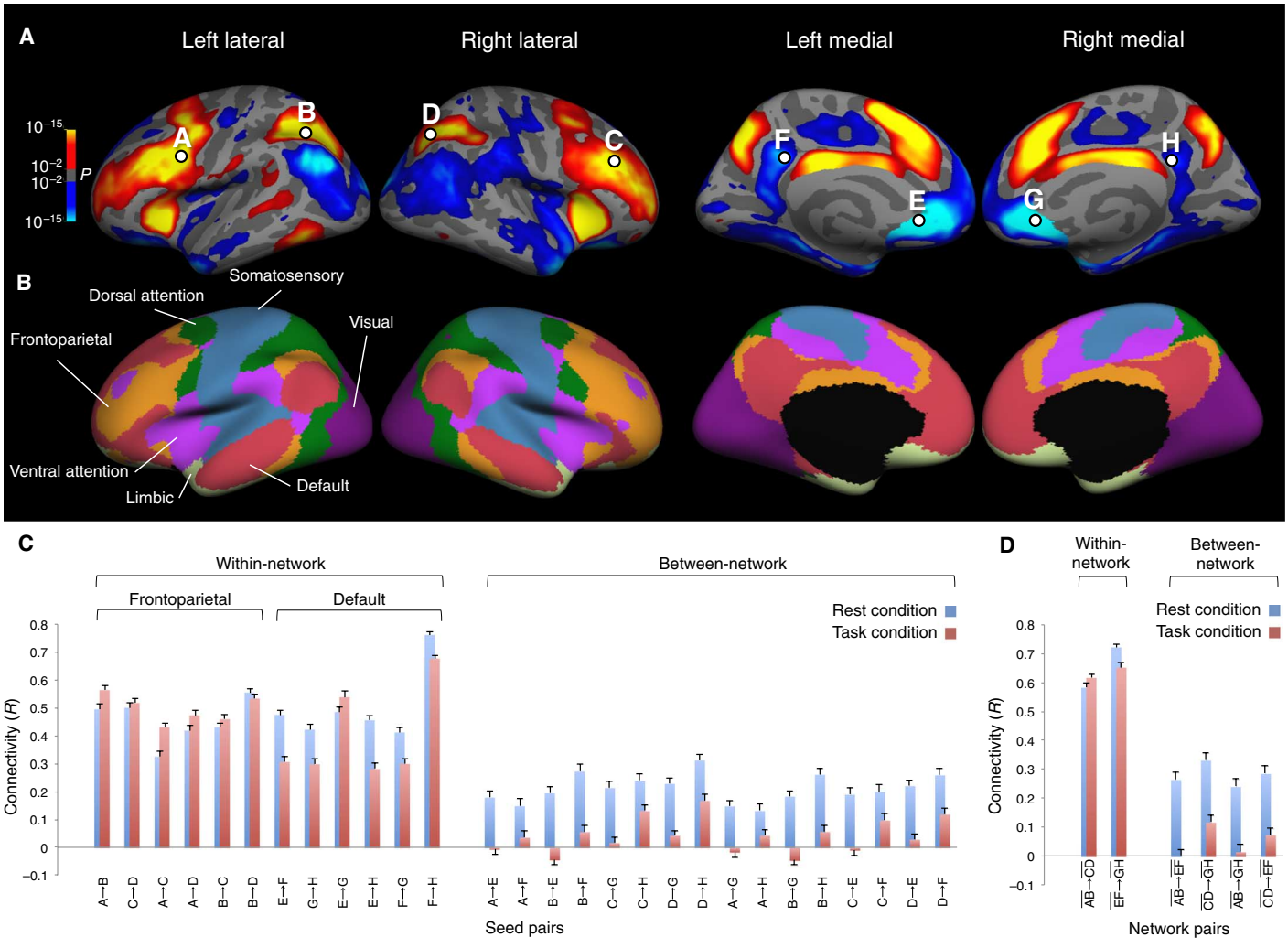


**Fig. 1. Working memory reflects changes in cortical network dynamics.** (**A**) Working memory performance robustly activates "task-positive" regions, including dlPFC (peaks at points A and C) and iPS (points B and D), and deactivates "task-negative" regions, including mPFC (points E and G) and pCing (points F and H). Maps are thresholded at the false discovery rate (FDR) ($q = 0.05$). (**B**) Activated regions correspond closely with FPCN, as previously defined (*20*) using resting-state data from 1000 healthy individuals (orange network), whereas deactivated regions fall largely within DN (red network). (**C**) Correlations of blood oxygen level–dependent (BOLD) signal time courses between seed pairs (for example, A→B represents left dlPFC to left iPS) indicates robust decoupling of FPCN and DN as subjects shift from rest to task condition (main effect of condition: $F = 55.7$, $P = 3.7 \times 10^{-11}$; main effect of within-/between-network: $F = 876$, $P = 2.3 \times 10^{-50}$; condition × within-/between-network interaction: $F = 56.3$, $P = 3.0 \times 10^{-11}$). (**D**) A similar pattern is seen using average BOLD signal time courses within FPCN ($\overline{AB}$ and $\overline{CD}$) and DN ($\overline{EF}$ and $\overline{GH}$) (main effect of condition: $F = 57.7$, $P = 1.9 \times 10^{-11}$; main effect of within-/between-network: $F = 928$, $P = 1.8 \times 10^{-51}$; condition × within-/between-network interaction: $F = 58.8$, $P = 1.4 \times 10^{-11}$). Bars indicate SE.

$D_1$ receptor density, we used the binding potential relative to the nondisplaceable compartment ($BP_{ND}$) obtained from analysis of the dynamic PET data (see Materials and Methods and fig. S2). We examined variation in $D_1$ receptor density across seven cortical networks using the parcellation previously derived by Yeo *et al.* (*20*). Mean $D_1$ density varied among individuals by approximately fourfold and also among network territories: highest density occurred in DN, followed by other association networks and then by primary sensory/motor networks (Fig. 2, A and B, and table S4A). However, $D_1$ densities across networks were tightly correlated; for example, individuals with high density in DN also exhibited high density in FPCN, despite the significant difference in mean density between these networks (Fig. 2C and table S4B). Accordingly, to reduce dimensionality for PET-MRI analyses, a single mean cortical $D_1$ density value was calculated for each subject. Mean cortical $D_1$ correlated weakly with mean striatal $D_1$ ($R = 0.36$, $P = 0.064$) (Fig. 2, D and E), consistent with the findings of Fujiwara *et al.* (*26*). Striatal $D_1$ correlated inversely with age ($R = -0.42$, $P = 0.03$), consistent with previous reports (*27*, *28*), but cortical $D_1$ was unrelated to age in this relatively young sample ($R = -0.08$, $P = 0.70$).

### Effects of $D_1$ receptor density on dynamic network connectivity

Immediately following NNC112 injection and during PET dynamic imaging, subjects underwent a resting-state fMRI scan and then task-based fMRI during SIRP performance (table S5), as in the $n = 100$ sample. fMRI data were excluded from one subject because of unacceptable head motion, leaving $n = 26$ for the PET-MRI analysis. Nodes in FPCN and DN were defined on the basis of peak vertices of activation or deactivation in the group map of working memory load-dependent activation, as before (fig. S3A and table S6). Substantial reductions in connectivity between FPCN and DN were again observed when subjects moved from rest to task conditions ($P < 10^{-5}$) (fig. S3B).

To assess the effects of risperidone administration on working memory and connectivity indices, 17 participants received medication-free conventional fMRI scans either before or after the PET-MRI session using the same MRI magnet (but without the PET insert). Compared to the conventional fMRI scans, working memory accuracy declined slightly and response time increased slightly during the PET-fMRI scan (fig. S4). However, no significant differences between scans were observed for resting- or task state connectivity (fig. S5).

We then determined whether variation in $D_1$ density predicted connectivity within and between FPCN and DN (Fig. 3 and table S7). Cortical $D_1$ was unrelated to connectivity within FPCN or DN during rest or task, but it predicted the degree of between-network decoupling between resting and task states (Fig. 3, A and B). The relationship between cortical $D_1$ density and network transitions from resting to task state was further evaluated by correlating $D_1$ with task minus rest connectivity, resulting in a pattern similar to the task state analysis. In contrast, striatal $D_1$ density showed an inverse correlation with resting-state connectivity within DN (left to right mPFC) (Fig. 3, C and D) but no relationship to FPCN or between-network connectivity. During task performance, striatal $D_1$ density correlated positively with connectivity within FPCN (right dlPFC to iPS) (Fig. 3E), consistent with previous work (*28*), but it did not predict DN or between-network connectivity. Neither cortical ($R = 0.07$, $P = .74$) nor striatal ($R = -0.14$, $P = .49$) $D_1$ density correlated with task accuracy across load conditions, consistent with previous studies of young, healthy individuals (*23*, *29*). Connectivity measures that were correlated significantly with $D_1$ density did not correlate significantly with task accuracy across load conditions ($-0.31 \leq R \leq 0.08$, $P > .10$).

Connectivity markers that showed significant relationships with either cortical or striatal $D_1$ density were further evaluated by partialing out effects of striatal or cortical $D_1$, respectively; for striatal correlations, effects of age were also partialed out (tables S8 and S9). These analyses demonstrated that cortical $D_1$ correlations were neither substantially influenced by effects of striatal $D_1$ or vice versa nor was age a confounding factor. As an additional control for network specificity of $D_1$ effects, we also evaluated whether $D_1$ density influenced coupling to the visual network, which was also differentially engaged between resting and task states (with subjects focusing, respectively, on a central fixation cross versus both central and peripheral targets). No relationship was found between cortical or striatal $D_1$ and decoupling of either FPCN or DN to the visual network (table S10).

## DISCUSSION

The dynamic interaction of task-negative networks such as DN and task-positive networks such as FPCN is thought to be critical for directing attentional resources away from internal stimuli and toward task engagement. Here, we directly associate crosstalk in working memory–related networks to cortical dopamine signaling in real time through the use of simultaneous PET and MRI scans. The key result is that low cortical $D_1$ density predicts stronger decoupling of FPCN and DN during working memory. The present findings also establish that dopaminergic modulation of working memory networks is pathway-specific because we observed divergent effects of $D_1$ receptors downstream of mesocorticolimbic versus nigrostriatal projections on within- and between-network interactions.

The observed effects of cortical $D_1$ signaling on network-level tuning are reminiscent of its established microcircuit-level effects during working memory (*2*–*4*). In studies of nonhuman primates, optimal levels of $D_1$ receptor stimulation suppress task-irrelevant inputs onto dendritic spines through a variety of mechanisms, including excitation of fast-spiking interneurons (*6*) and cyclic AMP (adenosine 5′-monophosphate)–mediated effects on hyperpolarization-activated cyclic nucleotide–gated cation channels (*5*, *7*). These cellular mechanisms potentially underlie $D_1$-mediated decoupling of DN and FPCN during working memory. That said, although the present results relate an index of cortical dopamine signaling to network dynamics, understanding the cellular physiology of this relationship requires additional study. Previous work has reported lower cortical $D_1$ density among individuals with putatively higher synaptic dopamine availability, such as those who carry the *COMT* 158Met allele (*22*). However, whether between-subject variation in $D_1$ receptor density reflects a compensatory response to chronic dopamine levels, polymorphisms in the *DRD1* gene (*30*), or a balance of these and other factors remains uncertain.

Consistent with previous studies of healthy individuals (*23*, *29*), we did not observe a significant relationship between $D_1$ receptor density and working memory performance; variation in performance was also unrelated to network decoupling. Normal variation in $D_1$ density and network decoupling thus appears insufficient to influence performance over the range of task difficulty that was tested. This pattern likely reflects the near-ceiling level of performance in most participants (even under the most difficult task conditions) and the normal range of cortical $D_1$ receptor density in this young, healthy cohort. However, studies

of individuals with cortical $D_1$ receptor densities that are higher (*23*) or lower (*27*) than those in healthy young individuals demonstrate linear relationships between $D_1$ receptor variation and performance measures. Similarly, studies that pharmacologically manipulate synaptic dopamine levels have demonstrated an inverted U relationship between cortical dopamine signaling and both local circuit function and working memory performance (*31*). It will be important to extend the present approach to study subjects who have a wider range of cortical $D_1$ density and to examine effects of acute manipulation of dopamine signaling. This work may determine whether performance deficits reflect effects of abnormal $D_1$ density and/or suboptimal synaptic dopamine concentrations on cortical network dynamics.

Following previously published methods (*25*), study participants were pretreated with risperidone to block NNC112 signal related to 5HT2a receptors. Whereas risperidone does not bind $D_1$ receptors, it is a $D_2$ receptor antagonist and may indirectly influence $D_1$ signaling through pre- and postsynaptic mechanisms. Notably, following risperidone administration, performance (accuracy and response time) was mildly impaired, but dynamic connectivity patterns were preserved. Whereas this pattern could suggest a dissociation between $D_1$ effects on connectivity and performance, it may also be the case that altered performance after risperidone treatment reflected independent mechanisms (most likely its direct antagonism of α2 adrenergic and histaminergic receptors, causing mild drowsiness) (*32*).

The present results raise questions about the regulation of $D_1$ receptor expression across cortical network territories. We observed a pattern of $D_1$ density differences between networks that was consistent across participants (that is, DN > other association networks > primary somatosensory networks); however, network $D_1$ density means were also interlinked to a surprising degree. These findings intimate both



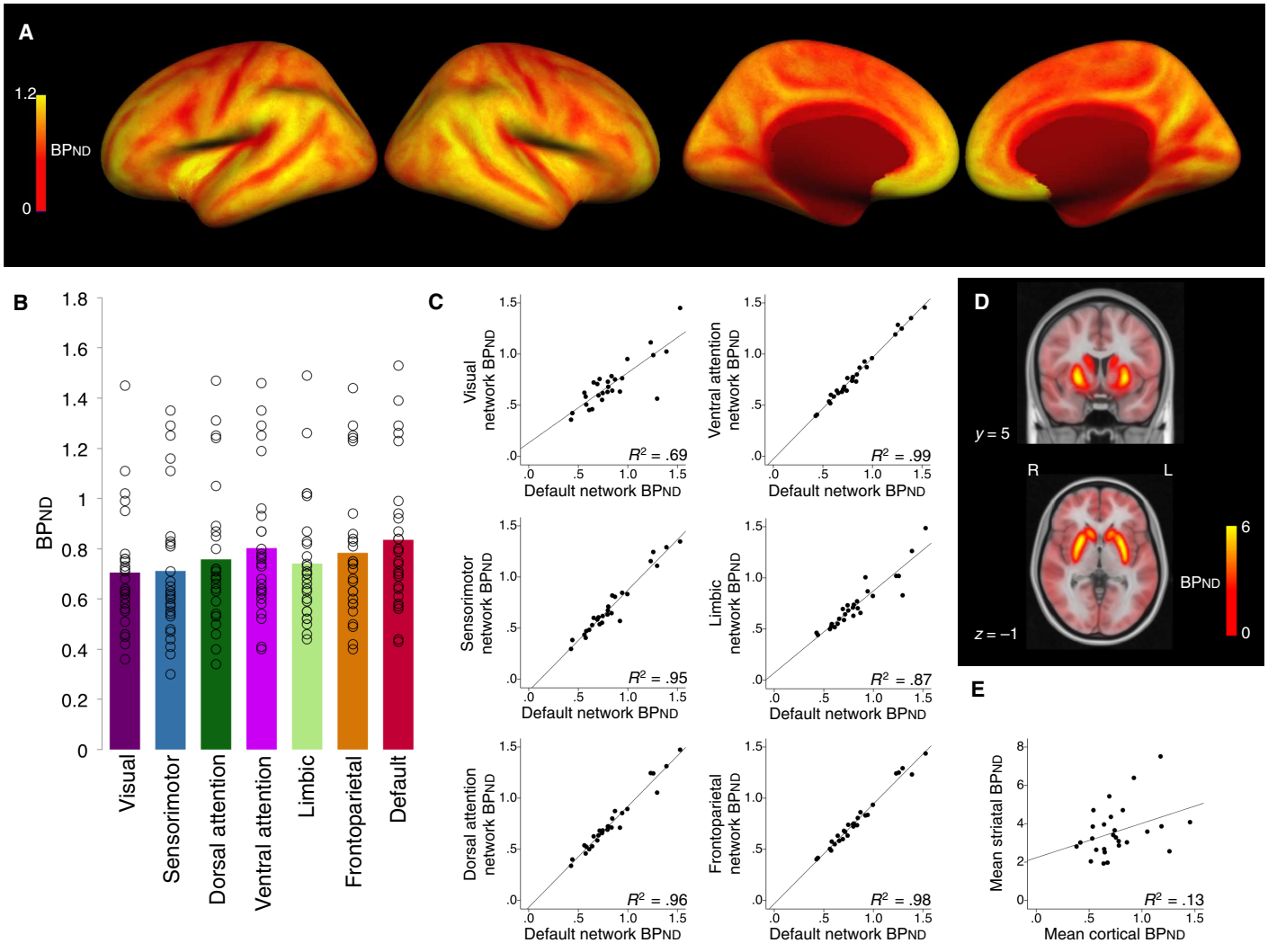


**Fig. 2. $D_1$ receptor density in cortical networks and striatum.** (**A**) Group average surface maps indicate mean density of $D_1$ receptors across the cortical mantle. (**B**) $D_1$ receptor density within seven cortical networks (circles are individual subjects, and bars are mean values), indicating a fourfold difference among individuals. Density within DN was higher than every other network ($P < 0.001$). (**C**) $D_1$ receptor density in DN correlated strongly with every other cortical network. (**D**) Coronal and horizontal views of group average volume map indicate striatal $D_1$ density. (**E**) Mean striatal $D_1$ density correlated weakly with mean cortical $D_1$ density ($R = 0.36$, $P = 0.064$).

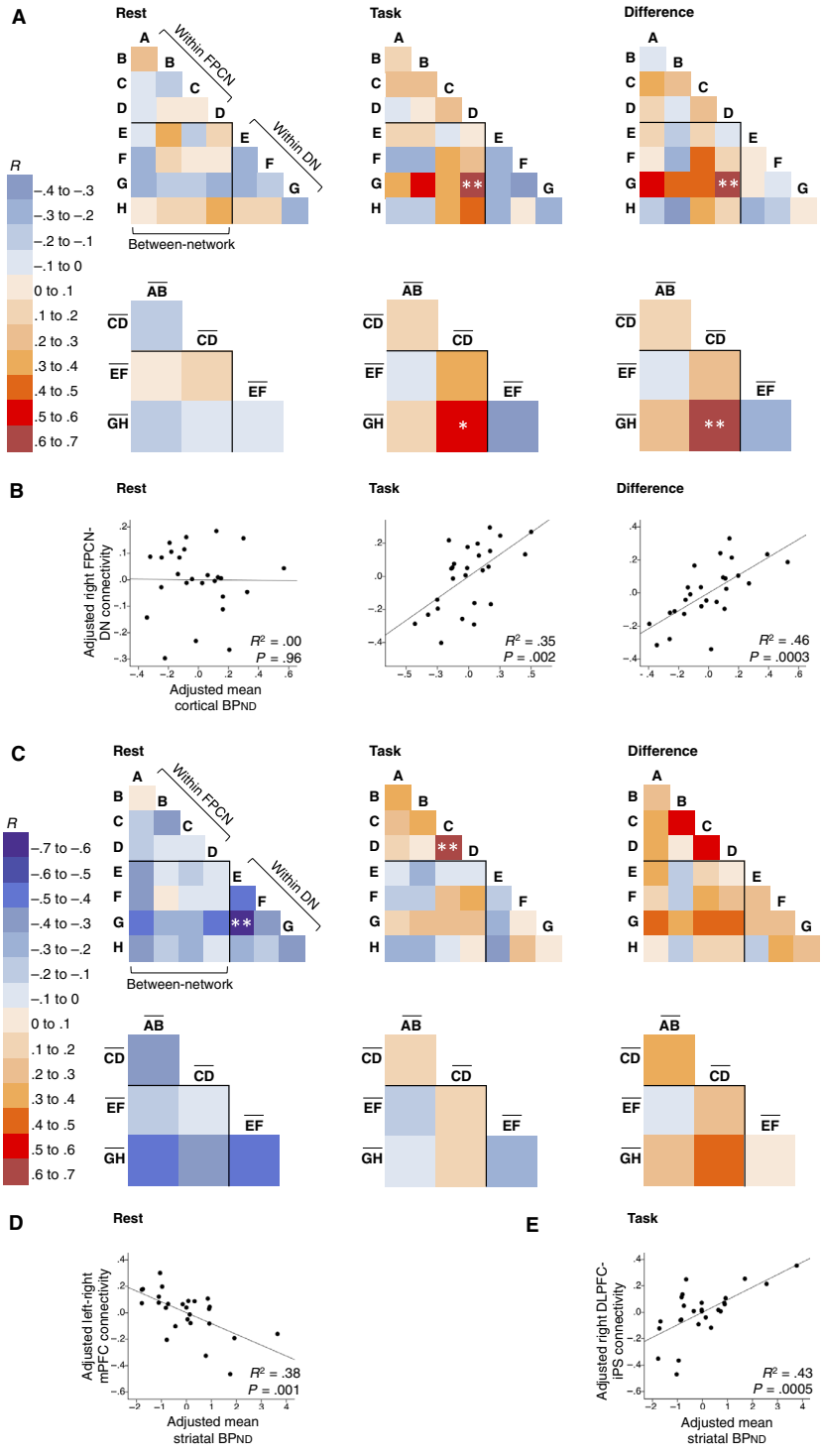


**Fig. 3. Contributions of cortical and striatal $D_1$ density to within- and between-network connectivity underlying working memory.** (**A**) Correlation matrices indicate the relationship between seed-to-seed (for example, A→B represents left dlPFC to left iPS) or network-to-network (for example, $\overline{AB}$→$\overline{CD}$ represents left FPCN to right FPCN) FC and cortical $D_1$ density. Between-network correlations are located inside the black lines, and within-network measurements are outside the black lines. (**B**) Lower cortical $D_1$ density predicted a greater decline in right FPCN to right DN connectivity between resting and task states. (**C**) Correlations of FC and striatal $D_1$ density, as in (A). (**D**) At rest, reduced striatal $D_1$ density predicted enhanced connectivity within DN (left mPFC to right mPFC). (**E**) During task, higher striatal $D_1$ density predicted stronger connectivity within FPCN (right dlPFC to right iPS). All analyses were adjusted for mean global signal and head motion. *$P$ < .05, FDR-corrected; **$P$ < .05, familywise error (FWE)–corrected.

network-specific and cortex-wide mechanisms regulating $D_1$ expression. Such complex topographic regulation likely reflects the interplay of specific genes, experience-dependent plasticity (*33*), and neurodevelopment (*34*). Given the degree of interrelatedness of $D_1$ receptor density across the cortex, it is difficult to ascribe regulation of network connectivity to any regionally specific patterns of $D_1$ signaling. Regional variation in cortical dopamine release may reflect important functional differences. For example, $D_1$ receptors in the mPFC are potentially more likely to process signal from value-oriented dopamine neurons that project preferentially to this region, whereas those in the dlPFC may be more likely to process signal from salience-oriented dopamine neurons (*35*). Such functional variation cannot be captured using $D_1$ PET ligands, which provide static measures of $D_1$ receptor density (*36*). Additional PET studies of dopamine synthesis, uptake, and release conducted in conjunction with fMRI could provide complementary mechanistic insights.

In summary, the present findings provide a foundation to explore how local and global changes in dopamine receptor expression scale to influence cortical network dynamics and, ultimately, cognitive performance. Furthermore, although the present study involved healthy individuals with intact working memory performance, this work may inform studies of how regionally specific disruptions in dopamine signaling impact cortical networks in schizophrenia (*11*) and other neuropsychiatric conditions characterized by working memory impairment.

## MATERIALS AND METHODS

### Study participants

Participants were healthy adult volunteers recruited through community advertisement. Two cohorts were enrolled: one group for conventional fMRI scans only ($n$ = 100; age range, 17 to 34 years; mean age, 24.2 years; 57 females and 43 males; 91 are right-handed) and a second, non-overlapping group for PET-MRI scans ($n$ = 29; age range, 20 to 51 years; mean age, 30.6 years; 11 females and 16 males; all are right-handed). Exclusion criteria for both studies included current Axis I psychiatric diagnosis [assessed through the Structured Clinical Diagnostic Interview for DSM-IV-TR (*Diagnostic and Statistical Manual of Mental Disorders, Fourth Edition, Text Revision)*, nonpatient version], current use of psychotropic medications, previous history of psychotic symptoms, current pregnancy, significant medical or neurological condition, or contraindication for MRI scanning (metallic implants and claustrophobia). In addition, PET-MRI participants were required to be right-handed, to have a normal physical and laboratory exam, and to have a negative serum pregnancy test on the day of scanning. PET-MRI participants also could not be actively nursing. Study procedures were approved by the Human Research Committee of Partners HealthCare, and all participants provided written informed consent.

### Working memory test

During the scan, participants underwent a modified version of the SIRP (*37*), a working memory test that focuses primarily on online maintenance of information (fig. S1). Repeated administration of the SIRP has not been associated with significant learning effects (*38*). E-Prime software was used to present stimuli to participants and to collect their responses. Each test block began with an encoding phase, consisting of presentation of one, three, five, or seven consonants (6 s). Following a brief delay epoch (2 s), subjects were asked to respond to 14 probes (consonants), each presented for 1.1 s and separated by a "jittered" intertrial interval of 0.6 to 2.5 s. Subjects were asked to indicate whether each probe was a target (one of the letters presented during the encoding phase; 50% of probes) or a foil (not presented during encoding; 50% of probes) by pressing the corresponding key on a button box being held in their dominant hand. Subjects underwent three runs of the task, each lasting 7 min 20 s and consisting of eight blocks (two blocks at each load level). Subjects practiced the task before scanning and were required to demonstrate above-chance performance.

### MRI acquisition

Participants in the conventional fMRI sample ($n$ = 100) were scanned using a Siemens 3T Skyra magnet and a 32-channel head coil. A high-resolution T1 image (repetition time/echo time/flip angle = 2530 ms/1.92 ms/7°) with an isotropic voxel size of $0.8 \times 0.8 \times 0.8$ mm$^3$ was acquired. Next, an interleaved multislice resting-state functional scan was collected using the following scan parameters: repetition time/echo time/flip angle = 1150 ms/30 ms/75°; in-plane resolution = 3 mm × 3 mm; slice thickness = 3 mm. Participants were instructed to keep their eyes open and remain still during the scan. Next, during the working memory task, a functional echo planar imaging (EPI) sequence was used with the following parameters: repetition time/echo time/flip angle = 2 s/30 ms/90°; in-plane resolution = 3.6 mm × 3.6 mm; slice thickness = 4 mm.

Participants in the PET-MRI cohort ($n$ = 29) were scanned using a Siemens 3T TIM Trio magnet equipped with a BrainPET insert and a PET-compatible circularly polarized transmit coil/eight-channel receive array coil. Ninety minutes before scanning, participants received 2 mg of oral risperidone to block nonspecific binding of NNC112 to 5HT2a receptors, consistent with previously published methods (*25*). A high-resolution T1 image (repetition time/echo time/flip angle = 2200 ms/1.54 ms/7°) with an isotropic voxel size of $1.2 \times 1.2 \times 1.2$ mm$^3$ was acquired. Next, a resting-state functional scan was collected using the following scan parameters: repetition time/echo time/flip angle = 3000 ms/30 ms/85°; in-plane resolution = 3 mm × 3 mm; slice thickness = 3 mm. Participants were instructed to keep their eyes open and remain still during the scan. Next, during the working memory task, a functional EPI sequence was used with the following parameters: repetition time/echo time/flip angle = 2 s/30 ms/90°; in-plane resolution = 3.6 mm × 3.6 mm; slice thickness = 3 mm.

Of the 29 PET-MRI participants, 17 also completed an optional second scan on a different day, using the same Siemens 3T TIM Trio magnet and the same scan sequence as the PET-MRI scan. This scan differed from the PET-MRI scan in that (i) participants were not pretreated with risperidone; (ii) the BrainPET insert was not positioned in the magnet; (iii) a standard 12-channel quadrature head coil was used; and (iv) the SIRP task used a different set of stimuli. Of these 17 participants, 11 first received the PET-MRI scan, and 6 first received the conventional fMRI scan.

### Anatomical MRI analysis

The T1 anatomical MRIs were analyzed in FreeSurfer (FS) version 5.3 (surfer.nmr.mgh.harvard.edu). FS performs a whole-brain segmentation of the T1 image including subcortical structures, such as hippocampus, amygdala, putamen, pallidum, caudate, nucleus accumbens, ventricles, and white matter (*39*). In addition, FS creates a mesh model of the cortical surfaces (*40*, *41*) as well as gyral labeling of cortex (*42*). FS also provides surface-based intersubject analysis (*43*). The FS anatomical analysis provided a substrate upon which the rest of the multimodal analysis is performed.

### fMRI analysis

All fMRI analysis was performed in the FS Functional Analysis Stream. The method was developed in the conventional fMRI cohort ($n$ = 100) and then repeated in the PET-MRI cohort ($n$ = 29). The fMRI analysis was divided into two parts. In the first part, the task-based data were analyzed to provide seed points for the individual analysis. In the second part, fMRI waveforms were extracted from the seeds; connectivity was quantified as the correlation coefficient between the waveforms. For the task-based analysis, the fMRI was motion-corrected, registered to the anatomical image (*44*), and resampled to the cortical surface where it was surface-smoothed by 5 mm (*45*). Runs where net head displacement was ≥0.1 mm per repetition time (TR; averaged over all volumes) were excluded; one subject in the PET-MRI cohort was excluded because the net head displacement was ≥0.1 mm per TR for all three working memory (SIRP) runs, leaving 28 subjects with usable task-based fMRI data (two of whom were subsequently excluded from the PET-MRI analysis because of premature PET scan termination). Time series analysis focused on blocks of the probe response phase, during which participants mentally scanned the memorized set, determined whether the letter probe belonged to the set, and executed a motor response. The individual time series analysis was performed using a parametric modulation technique in which the linear slope of the probe activation versus working memory load was estimated at each vertex for each subject. At the group level, the group mean slope was tested for a difference from zero at each vertex in the surface-based common space (analogous to Montreal Neurological Institute volume space) to yield the statistical maps shown in Fig. 1A and fig. S3A.

### Seed placement

Peak vertices of working memory load-dependent task activation or deactivation within FPCN and DN were used to localize seeds for FC analysis. FPCN peaks included left dlPFC (seed "A"), left iPS (seed "B"), right dlPFC (seed "C"), and right iPS (seed "D"); and DN peaks included left mPFC (seed "E"), left pCing (seed "F"), right mPFC (seed "G"), and right pCing (seed "H"). For each peak vertex, a seed region was created on the surface by dilating a disc centered on the peak vertex to a radius of approximately 6 mm, using smoothing and binarization that were applied in the same way for each seed. This seed region was then mapped to each individual subject through the surface-based intersubject registration (*43*). The region was then mapped to the fMRI space of the individual through the anatomical-functional registration to identify voxels in the fMRI volume that belong to the seed. Thus, seeds represented semi-individualized regions composed of only gray matter. Eight such seeds centered on peak vertices within FPCN and DN from the task-related analysis (tables S2 and S6) were then generated for the connectivity analysis. For the PET-MRI cohort, the process was repeated for four additional seeds within the visual network adapted from the study of Yeo *et al.* (*20*), corresponding to left V1p (seed "W"), left V1c (seed "X"), right V1p (seed "Y"), and right V1c (seed "Z"), for control analyses.

### FC analysis

FC analysis was performed in an identical manner for both task and resting-state fMRI. The first of the three task blocks was used for FC analysis because it immediately followed the resting-state scan and facilitated comparisons of resting-to-task state transitions. To further minimize movement-related artifacts, we determined whether any time points exhibited head motion of ≥1.5 mm in any direction. No such time points were found in the $n$ = 100 conventional fMRI sample. For the PET-MRI cohort, one subject exhibited motion of ≥1.5 mm during three of the last four time points of their SIRP run; the last four time points were therefore subsequently removed from the analysis. A time series waveform for each seed was generated by averaging the time series of the voxels in the seed from the motion-corrected fMRI volume. For both rest and task runs, pairwise seed-to-seed connectivity for each subject was computed as the Pearson's $R$ between the time series of the two seeds. For example, the connectivity of the A→B pair (left dlPFC to left iPS) during the rest scan was determined by calculating the Pearson coefficient for the time series extracted from the "A" and "B" seeds. To better assess connectivity within and between networks, mean time courses were calculated for each subject for the following pairs:

"A" and "B" ("$\overline{AB}$," corresponding to left FPCN)
"C" and "D" ("$\overline{CD}$," corresponding to right FPCN)
"E" and "F" ("$\overline{EF}$," corresponding to left DN)
"G" and "H" ("$\overline{GH}$," corresponding to right DN)
"W" and "X" ("$\overline{WX}$," corresponding to left visual network, in PET-MRI scans)
"Y" and "Z" ("$\overline{YZ}$," corresponding to right visual network, in PET-MRI scans)

Within-network connectivity values (for example, $\overline{AB} \rightarrow \overline{CD}$, corresponding to left FPCN to right FPCN) and between-network connectivity values (for example, $\overline{AB} \rightarrow \overline{EF}$, corresponding to left FPCN to left DN) were computed by correlating the respective mean network time courses using Pearson's $R$.

### Radiotracer synthesis

NNC112 was prepared by $N$-methylation of the precursor using [$^{11}$C] methyl iodide, analogous to that previously described by Halldin *et al.* (*46*). Radiotracer use was approved by the Massachusetts General Hospital Radioactive Drug Research Committee.

### PET acquisition, processing, and image reconstruction

PET data were acquired using the Siemens BrainPET scanner (*47*). This prototype device is a head-only PET insert that fits in the bore of the 3T TIM Trio MRI scanner. The BrainPET detector module consists of a 12 × 12 array of 2.5 × 2.5 × 20–mm$^3$ lutetium oxyorthosilicate crystals readout by a 3 × 3 array of magnetic field–insensitive avalanche photodiodes. Emission data were acquired in list-mode format for 90 min following the intravenous administration of 9.59 ± 1.65 mCi (range, 5.07 to 11.96 mCi) of NNC112. For each coincidence event, the line of response joining the two crystals in which the two 511-keV photons were detected was rebinned into sinogram space using nearest neighbor approximation and axial compression (span, 9; maximum ring difference, 67). Each sinogram consisted of 192 angular projections and 256 radial elements. The calculation of random coincidences was performed by sorting the delayed coincidences into delayed single maps, from which the total singles rate as well as the variance reduced randoms were estimated (*48*). The sensitivity data were acquired with a plane source scanned in 16 positions (with a 22.5° angular step), 4 hours per position, and the normalization sinogram was derived from these data. The head attenuation map was generated from the MRI data (*49*). The scatter coincidence sinogram was obtained using a calculated method based on the single scatter estimation method (*50*).

To correct for head motion over the duration of the scan, head motion estimates were derived offline from the MRI data for all of the EPI-based acquisitions. When MRI data were unavailable (for example, for

non–EPI-based acquisitions), a PET-based method was used to derive motion estimates with a temporal resolution of 60 s during the first 40 min, and 120 s for the remainder of the scan. The combined motion estimates were used to correct the dynamic PET frames before image reconstruction (*51*). For this purpose, the list-mode data set was first divided into frames of variable duration according to the pharmacokinetic protocol (that is, 8 × 10, 3 × 20, 2 × 30, 1 × 60, 1 × 120, 1 × 180, 8 × 300, and 4 × 600 s). Motion correction was subsequently applied separately to each of these frames. The head attenuation and scatter correction sinograms were estimated only in the reference frame. The motion-corrected PET volumes corresponding to each of the frames were reconstructed using the standard Ordinary Poisson Ordered Subset Expectation Maximization three-dimensional (3D) algorithm from motion-corrected prompt and random coincidences, normalization, attenuation, and scatter coincidence sinograms using 16 subsets and six iterations. The implementation has been revisited for improving the speed, allowing a full 3D calculation (*52*). The reconstructed volume consisted of 153 slices with 256 × 256 pixels (1.25 × 1.25 × 1.25 $mm^3$).

### Arterial input function measurement

Arterial sampling was successfully performed in 25 of the 27 subjects. For two subjects, arterial canulation was unsuccessful after several efforts. A licensed anesthesiologist placed a catheter in the radial artery proximal to the wrist under local anesthesia, and samples were drawn from an 8-inch extension tube by an experienced research nurse using a vacutainer system into heparinized evacuated blood collection tubes. Samples (2 ml) were drawn by hand every 10 s for the first 3 min postinjection. Subsequently, 6-ml samples were drawn (after a 6-ml discard) at 5, 10, 20, 30, 60, and 90 min postinjection. For NNC112 blood analysis, a 300-μl sample of whole blood was pipetted from each collection tube, and the activity was counted using a γ counter (Wizard$^2$ 2480, PerkinElmer). The parent fraction was also measured from the last six samples using a method described previously (*21*). The whole-blood and parent fraction curves were modeled using a piecewise linear and three and two exponential functions, respectively. All counts were decay-corrected to the time of injection.

### PET image processing

Post-reconstruction partial volume effects correction was applied to the motion-corrected PET images using a region-based voxelwise method (*53*) and modeling the spatially variant point spread function through the convolution of a spatially invariant 3-mm full width at half maximum (FWHM) Gaussian kernel and a radial motion blurring function (with a motion blur parameter of 16) (*45*). The regions of interest (ROIs) used for partial volume effects correction were obtained by combining regions derived from the FS segmentation and those derived from the analysis of the fMRI data collected using the same contrast (working memory load-dependent activation during the SIRP) in a different group of 50 subjects. The cortical ribbon was smoothed with a 10-mm FWHM Gaussian kernel using a surface-based method (*46*). For this purpose, the corresponding voxels were mapped to the surface using FS, smoothing was performed on the surface, and the inverse mapping was applied to move the voxels in the original PET space. Volumetric smoothing with a 3-mm FWHM Gaussian kernel was applied to the subcortical regions.

The $BP_{ND}$ (*54*) was the primary outcome measure in this study. Regional and pixelwise analyses were performed using PMOD (PMOD Technologies Ltd.). $BP_{ND}$ was estimated in two ways: using the Logan reference tissue model (*55*) and using the Logan plot and the measured arterial input function (AIF) (*56*). The reference tissue model was implemented and validated so that all 27 subjects, including those for whom arterial blood sampling was not performed, could be included. The cerebellar cortex, which is devoid of $D_1$ receptors (*57*), was used as the reference region (*55*). For the AIF method, regional distribution volumes ($V_T$) were first derived for 18 regions of interest by graphical analysis using the time-activity curves obtained by taking the mean of each of the regions and the measured AIF (*56*). In addition to bilateral cerebellar cortex, caudate, and putamen, the following bilateral cortical regions were defined on the basis of the MRI data: dorsolateral prefrontal, dorsal cingulate, temporal, pCing, iPS, and insula. The $BP_{ND}$ for each ROI was estimated as [$V_T$ (ROI)/$V_T$ (cerebellum) − 1] (*58*). Among the 16 noncerebellar ROIs, correlation coefficients for AIF versus reference tissue models consistently indicated a strong relationship ($0.82 \leq R^2 \leq 0.99$; mean $R^2$ across 16 regions = 0.96) (see fig. S2). Finally, pixelwise parametric maps of the $BP_{ND}$ were generated from the surface/volumetric smoothed PET data of all 27 subjects using the Logan reference model (*55*) with the cerebellar cortex as the reference.

### Statistical analysis

**Within- versus between-network connectivity.** For each condition (rest and task), mean within- and between-network connectivity was calculated for each subject by averaging the seed-to-seed pairwise time course correlations (that is, within-network correlations included A→B, A→C, A→D, B→C, B→D, C→D, E→F, E→G, E→H, F→G, F→H, and G→H; between-network correlations included A→E, A→F, A→G, A→H, B→E, B→F, B→G, B→H, C→E, C→F, C→G, C→H, D→E, D→F, D→G, and D→H). Then, repeated-measures analysis of variance (ANOVA) was used to assess the main effects of condition (rest versus task), network category (within versus between), and their interaction, covarying for *z*-transformed mean global signal and head motion (defined as mean net displacement per TR). The analysis was repeated using averaged time courses within networks (that is, within-network correlations included $\overline{AB}$→$\overline{CD}$ and $\overline{EF}$→$\overline{GH}$; between-network correlations included $\overline{AB}$→$\overline{EF}$, $\overline{AB}$→$\overline{GH}$, $\overline{CD}$→$\overline{EF}$, and $\overline{CD}$→$\overline{GH}$).

**$D_1$ density–connectivity correlations.** Each seed-to-seed and network-to-network connectivity measure was correlated with striatal $D_1$ density for rest and task scans, as well as for task minus rest (34 $D_1$ density–connectivity comparisons per condition), partialing out condition-specific *z*-transformed mean global signal and head motion, as above. Significant ($P < 0.05$, corrected) correlations were identified after FWE was used to control for multiple comparisons within each condition. Because of the lack of independence of many connectivity measures, correction using FDR ($q = 0.05$) was also attempted to reduce the risk of type II error. The process was repeated for cortical $D_1$ density correlations. Significant $D_1$ density–connectivity relationships were further evaluated with additional partial correlations to control for the correlation of striatal and cortical $D_1$ densities and for the correlation of striatal $D_1$ density with age.

**Effects of risperidone on working memory performance and connectivity.** For the 17 PET-MRI participants who also underwent a second conventional fMRI scan without risperidone pretreatment, effects of risperidone on SIRP performance were evaluated using repeated-measures ANOVA, with medication status (on versus off risperidone) and accuracy (% correct at one, three, five, and seven items) as within-subject factors and scan order (PET-MRI scan first versus conventional fMRI scan first) as a between-subjects factor. The analysis

was repeated for SIRP response time. An analogous analysis was used to determine whether there were effects of risperidone on connectivity measures. Repeated-measures ANOVA evaluated medication status (on versus off risperidone), condition (rest versus task), and each connectivity measurement as within-subject factors, scan order as a between-subject factor, and scan-specific $z$-transformed mean global signal and motion as covariates.

## SUPPLEMENTARY MATERIALS

Supplementary material for this article is available at http://advances.sciencemag.org/cgi/content/full/2/6/e1501672/DC1

fig. S1. Working memory paradigm.
fig. S2. Validation of $BP_{ND}$ measurements derived from cerebellar reference model against arterial input model.
fig. S3. Working memory–related activation and connectivity changes in PET-MRI cohort.
fig. S4. Reliability of performance measures between conventional fMRI and PET-MRI scans.
fig. S5. Reliability of connectivity measures between conventional fMRI and PET-MRI scans.
table S1. Working memory performance in $n$ = 100 fMRI cohort.
table S2. Nodes for connectivity analysis in $n$ = 100 fMRI cohort.
table S3. Local correlations of task-based activation with connectivity during rest and task.
table S4. $D_1$ density relationships among cortical networks.
table S5. Working memory performance in $n$ = 29 PET-MRI cohort.
table S6. Nodes for connectivity analysis in $n$ = 29 PET-MRI cohort.
table S7. Correlations of PET and fMRI connectivity (FPCN and DN) markers across conditions.
table S8. Persistence of significant ($P < 0.05$, FWE-corrected) cortical $D_1$ density–connectivity correlations after partialing out effects of striatal $D_1$ density.
table S9. Persistence of significant ($P < 0.05$, FWE-corrected) striatal $D_1$ density–connectivity correlations after partialing out effects of age and cortical $D_1$ density.
table S10. Correlations of PET and fMRI connectivity (FPCN and DN to visual network) markers across conditions.

## REFERENCES AND NOTES


1. M. D. Fox, A. Z. Snyder, J. L. Vincent, M. Corbetta, D. C. Van Essen, M. E. Raichle, The human brain is intrinsically organized into dynamic, anticorrelated functional networks. *Proc. Natl. Acad. Sci. U.S.A.* **102**, 9673–9678 (2005).
2. T. Sawaguchi, P. S. Goldman-Rakic, D1 dopamine receptors in prefrontal cortex: Involvement in working memory. *Science* **251**, 947–950 (1991).
3. G. V. Williams, P. S. Goldman-Rakic, Modulation of memory fields by dopamine D1 receptors in prefrontal cortex. *Nature* **376**, 572–575 (1995).
4. A. F. T. Arnsten, M. Wang, C. D. Paspalas, Dopamine's actions in primate prefrontal cortex: Challenges for treating cognitive disorders. *Pharmacol. Rev.* **67**, 681–696 (2015).
5. N. J. Gamo, G. Lur, M. J. Higley, M. Wang, C. D. Paspalas, S. Vijayraghavan, Y. Yang, B. P. Ramos, K. Peng, A. Kata, L. Boven, F. Lin, L. Roman, D. Lee, A. F. T. Arnsten, Stress impairs prefrontal cortical function via $D_1$ dopamine receptor interactions with hyperpolarization-activated cyclic nucleotide-gated channels. *Biol. Psychiatry* **78**, 860–870 (2015).
6. S. Kröner, L. S. Krimer, D. A. Lewis, G. Barrionuevo, Dopamine increases inhibition in the monkey dorsolateral prefrontal cortex through cell type–specific modulation of interneurons. *Cereb. Cortex* **17**, 1020–1032 (2007).
7. S. Vijayraghavan, M. Wang, S. G. Birnbaum, G. V. Williams, A. F. T. Arnsten, Inverted-U dopamine D1 receptor actions on prefrontal neurons engaged in working memory. *Nat. Neurosci.* **10**, 376–384 (2007).
8. J. K. Seamans, C. R. Yang, The principal features and mechanisms of dopamine modulation in the prefrontal cortex. *Prog. Neurobiol.* **74**, 1–58 (2004).
9. H.-Y. Tan, J. H. Callicott, D. R. Weinberger, Dysfunctional and compensatory prefrontal cortical systems, genes and the pathogenesis of schizophrenia. *Cereb. Cortex* **17** (suppl. 1), i171–i181 (2007).
10. L. Bäckman, S. Karlsson, H. Fischer, P. Karlsson, Y. Brehmer, A. Rieckmann, S. W. S. MacDonald, L. Farde, L. Nyberg, Dopamine $D_1$ receptors and age differences in brain activation during working memory. *Neurobiol. Aging* **32**, 1849–1856 (2011).
11. M. Slifstein, E. van de Giessen, J. Van Snellenberg, J. L. Thompson, R. Narendran, R. Gil, E. Hackett, R. Girgis, N. Ojeil, H. Moore, D. D'Souza, R. T. Malison, Y. Huang, K. Lim, N. Nabulsi, R. E. Carson, J. A. Lieberman, A. Abi-Dargham, Deficits in prefrontal cortical and extrastriatal dopamine release in schizophrenia: A positron emission tomographic functional magnetic resonance imaging study. *JAMA Psychiatry* **72**, 316–324 (2015).
12. R. D. Oades, G. M. Halliday, Ventral tegmental (A10) system: Neurobiology. 1. Anatomy and connectivity. *Brain Res.* **434**, 117–165 (1987).
13. D. Tomasi, N. D. Volkow, Functional connectivity of substantia nigra and ventral tegmental area: Maturation during adolescence and effects of ADHD. *Cereb. Cortex* **24**, 935–944 (2014).
14. A. Nagano-Saito, J. Liu, J. Doyon, A. Dagher, Dopamine modulates default mode network deactivation in elderly individuals during the Tower of London task. *Neurosci. Lett.* **458**, 1–15 (2009).
15. C. G. Wong, M. C. Stevens, The effects of stimulant medication on working memory functional connectivity in attention-deficit/hyperactivity disorder. *Biol. Psychiatry* **71**, 458–466 (2012).
16. A. Rieckmann, S. Karlsson, H. Fischer, L. Bäckman, Increased bilateral frontal connectivity during working memory in young adults under the influence of a dopamine D1 receptor antagonist. *J. Neurosci.* **32**, 17067–17072 (2012).
17. E. M. Gordon, M. Stollstorff, J. M. Devaney, S. Bean, C. J. Vaidya, Effect of dopamine transporter genotype on intrinsic functional connectivity depends on cognitive state. *Cereb. Cortex* **22**, 2182–1296 (2012).
18. E. M. Tunbridge, S. M. Farrell, P. J. Harrison, C. E. Mackay, Catechol-O-methyltransferase (COMT) influences the connectivity of the prefrontal cortex at rest. *Neuroimage* **68**, 49–54 (2013).
19. C. Y. Sander, J. M. Hooker, C. Catana, M. D. Normandin, N. M. Alpert, G. M. Knudsen, W. Vanduffel, B. R. Rosen, J. B. Mandeville, Neurovascular coupling to D2/D3 dopamine receptor occupancy using simultaneous PET/functional MRI. *Proc. Natl. Acad. Sci. U.S.A.* **110**, 11169–11174 (2013).
20. B. T. T. Yeo, F. M. Krienen, J. Sepulcre, M. R. Sabuncu, D. Lashkari, M. Hollinshead, J. L. Roffman, J. W. Smoller, L. Zöllei, J. R. Polimeni, B. Fischl, H. Liu, R. L. Buckner, The organization of the human cerebral cortex estimated by functional connectivity. *J. Neurophysiol.* **106**, 1125–1165 (2011).
21. A. Abi-Dargham, D. Martinez, O. Mawlawi, N. Simpson, D.-R. Hwang, M. Slifstein, S. Anjilvel, J. Pidcock, N.-N. Guo, I. Lombardo, J. J. Mann, R. Van Heertum, C. Foged, C. Halldin, M. Laruelle, Measurement of striatal and extrastriatal dopamine $D_1$ receptor binding potential with [$^{11}$C]NNC 112 in humans: Validation and reproducibility. *J. Cereb. Blood Flow Metab.* **20**, 225–243 (2000).
22. M. Slifstein, B. Kolachana, E. H. Simpson, P. Tabares, B. Cheng, M. Duvall, W. Gordon Frankle, D. R. Weinberger, M. Laruelle, A. Abi-Dargham, COMT genotype predicts cortical-limbic D1 receptor availability measured with [$^{11}$C]NNC112 and PET. *Mol. Psychiatry* **13**, 821–827 (2008).
23. A. Abi-Dargham, O. Mawlawi, I. Lombardo, R. Gil, D. Martinez, Y. Huang, D.-R. Hwang, J. Keilp, L. Kochan, R. Van Heertum, J. M. Gorman, M. Laruelle, Prefrontal dopamine $D_1$ receptors and working memory in schizophrenia. *J. Neurosci.* **22**, 3708–3719 (2002).
24. J. Ekelund, M. Slifstein, R. Narendran, O. Guillin, H. Belani, N.-N. Guo, Y. Hwang, D.-R. Hwang, A. Abi-Dargham, M. Laruelle, *In vivo* DA $D_1$ receptor selectivity of NNC 112 and SCH 23390. *Mol. Imaging Bio.* **9**, 117–125 (2007).
25. M. Slifstein, L. S. Kegeles, R. Gonzales, W. G. Frankle, X. Xu, M. Laruelle, A. Abi-Dargham, [$^{11}$C]NNC 112 selectivity for dopamine $D_1$ and serotonin 5-$HT_{2A}$) receptors: A PET study in healthy human subjects. *J. Cereb. Blood Flow Metab.* **27**, 1733–1741 (2007).
26. H. Fujiwara, H. Ito, F. Kodaka, Y. Kimura, H. Takano, T. Suhara, Association between striatal subregions and extrastriatal regions in dopamine $D_1$ receptor expression: A positron emission tomography study. *PLOS One* **7**, e49775 (2012).
27. S. W. MacDonald, S. Karlsson, A. Rieckmann, L. Nyberg, L. Bäckman, Aging-related increases in behavioral variability: Relations to losses of dopamine $D_1$ receptors. *J. Neurosci.* **32**, 8186–8191 (2012).
28. A. Rieckmann, S. Karlsson, H. Fischer, L. Bäckman, Caudate dopamine D1 receptor density is associated with individual differences in frontoparietal connectivity during working memory. *J. Neurosci.* **31**, 14284–14290 (2011).
29. S. Karlsson, A. Rieckmann, P. Karlsson, L. Farde, L. Nyberg, L. Bäckman, Relationship of dopamine D1 receptor binding in striatal and extrastriatal regions to cognitive functioning in healthy humans. *Neuroimage* **57**, 346–351 (2011).
30. J. Yao, M. Ding, H. Pang, J.-X. Xing, J.-F. Xuan, B.-J. Wang, Dopamine D1 receptor (DRD1) 5′ region haplotypes significantly affect transcriptional activity in vitro. *Neurosci. Lett.* **609**, 120–123 (2015).
31. R. Cools, M. D'Esposito, Inverted-U–shaped dopamine actions on human working memory and cognitive control. *Biol. Psychiatry* **69**, e113–e125 (2011).
32. N. A. Keks, C. Culhane, Risperidone (Risperdal): clinical experience with a new antipsychosis drug. *Expert Opin. Investig. Drugs* **8**, 443–452 (1999).
33. F. McNab, A. Varrone, L. Farde, A. Jucaite, P. Bystritsky, H. Forssberg, T. Klingberg, Changes in cortical dopamine D1 receptor binding associated with cognitive training. *Science* **323**, 800–802 (2009).
34. S. L. Andersen, A. T. Thompson, M. Rutstein, J. C. Hostetter, M. H. Teicher, Dopamine receptor pruning in prefrontal cortex during the periadolescent period in rats. *Synapse* **37**, 167–169 (2000).
35. E. S. Bromberg-Martin, M. Matsumoto, O. Hikosaka, Dopamine in motivational control: Rewarding, aversive, and alerting. *Neuron* **68**, 815–834 (2010).
36. S. J. Finnema, B. Bang-Andersen, M. Jørgensen, C. T. Christoffersen, B. Gulyás, H. V. Wikström, L. Farde, C. Halldin, The dopamine $D_1$ receptor agonist (S)-[$^{11}$C]*N*-methyl-NNC 01-0259 is

not sensitive to changes in dopamine concentration—A positron emission tomography examination in the monkey brain. *Synapse* **67**, 586–595 (2013).
37. S. Sternberg, High-speed scanning in human memory. *Science* **153**, 652–654 (1966).
38. M. W. Kristofferson, Effects of practice on character-classification performance. *Can. J. Psychiatry* **26**, 54–60 (1972).
39. B. Fischl, D. H. Salat, E. Busa, M. Albert, M. Dieterich, C. Haselgrove, A. van der Kouwe, R. Killiany, D. Kennedy, S. Klaveness, A. Montillo, N. Makris, B. Rosen, A. M. Dale, Whole brain segmentation: Automated labeling of neuroanatomical structures in the human brain. *Neuron* **33**, 341–355 (2002).
40. A. M. Dale, B. Fischl, M. I. Sereno, Cortical surface-based analysis. I: Segmentation and surface reconstruction. *Neuroimage* **9**, 179–194 (1999).
41. B. Fischl, M. I. Sereno, A. M. Dale, Cortical surface-based analysis. II: Inflation, flattening, and a surface-based coordinate system. *Neuroimage* **9**, 195–207 (1999).
42. B. Fischl, A. van der Kouwe, C. Destrieux, E. Halgren, F. Ségonne, D. H. Salat, E. Busa, L. J. Seidman, J. Goldstein, D. Kennedy, V. Caviness, N. Makris, B. Rosen, A. M. Dale, Automatically parcellating the human cerebral cortex. *Cereb. Cortex* **14**, 11–22 (2004).
43. B. Fischl, M. I. Sereno, R. B. Tootell, A. M. Dale, High-resolution intersubject averaging and a coordinate system for the cortical surface. *Hum. Brain Mapp.* **8**, 272–284 (1999).
44. D. N. Greve, B. Fischl, Accurate and robust brain image alignment using boundary-based registration. *Neuroimage* **48**, 63–72 (2009).
45. D. J. Hagler Jr., A. P. Saygin, M. I. Sereno, Smoothing and cluster thresholding for cortical surface-based group analysis of fMRI data. *Neuroimage* **33**, 1093–1103 (2006).
46. C. Halldin, C. Foged, Y.-H. Chou, P. Karlsson, C.-G. Swahn, J. Sandell, G. Sedvall, L. Farde, Carbon-11-NNC 112: A radioligand for PET examination of striatal and neocortical $D_1$-dopamine receptors. *J. Nucl. Med.* **39**, 2061–2068 (1998).
47. H.-P. W. Schlemmer, B. J. Pichler, M. Schmand, Z. Burbar, C. Michel, R. Ladebeck, K. Jattke, D. Townsend, C. Nahmias, P. K. Jacob, W.-D. Heiss, C. D. Claussen, Simultaneous MR/PET imaging of the human brain: Feasibility study. *Radiology* **248**, 1028–1035 (2008).
48. L. G. Byars, M. Sibomana, Z. Burbar, J. Jones, V. Panin, W. C. Barker, J.-S. Liow, R. E. Carson, C. Michel, *Variance reduction on randoms from delayed coincidence histograms for the HRRT*. Proc. IEEE Medical Imaging Conf. **5**, 2622–2626 (2005).
49. D. Izquierdo-Garcia, K. T. Chen, A. E. Hansen, S. Förster, D. Benoit, S. Schachoff, S. Fürst, D. B. Chonde, C. Catana, New SPM8-based MRAC method for simultaneous PET/MR brain images: Comparison with state-of-the-art non-rigid registration methods. *EJNMMI Phys.* **1**, A29 (2014).
50. C. C. Watson, New, faster, image-based scatter correction for 3D PET. *IEEE Trans. Nucl. Sci.* **3**, 1637–1641 (1999).
51. C. Catana, T. Benner, A. van der Kouwe, L. Byars, M. Hamm, D. B. Chonde, C. J. Michel, G. El Fakhri, M. Schmand, A. G. Sorensen, MRI-assisted PET motion correction for neurologic studies in an integrated MR-PET scanner. *J. Nucl. Med.* **52**, 154–161 (2011).
52. I. K. Hong, S. T. Chung, H. K. Kim, Y. B. Kim, Y. D. Son, Z. H. Cho, Ultra fast symmetry and SIMD-based projection-backprojection (SSP) algorithm for 3-D PET image reconstruction. *IEEE Trans. Med. Imaging* **26**, 789–803 (2007).
53. B. A. Thomas, K. Erlandsson, M. Modat, L. Thurfjell, R. Vandenberghe, S. Ourselin, B. F. Hutton, The importance of appropriate partial volume correction for PET quantification in Alzheimer's disease. *Eur. J. Nuc. Med. Mol. Imaging* **38**, 1104–1119 (2011).
54. R. B. Innis, V. J. Cunningham, J. Delforge, M. Fujita, A. Gjedde, R. N. Gunn, J. Holden, S. Houle, S.-C. Huang, M. Ichise, H. Iida, H. Ito, Y. Kimura, R. A. Koeppe, G. M. Knudsen, J. Knuuti, A. A. Lammertsma, M. Laruelle, J. Logan, R. P. Maguire, M. A. Mintun, E. D. Morris, R. Parsey, J. C. Price, M. Slifstein, V. Sossi, T. Suhara, J. R. Votaw, D. F. Wong, R. E. Carson, Consensus nomenclature for *in vivo* imaging of reversibly binding radioligands. *J. Cereb. Blood Flow Metab.* **27**, 1533–1539 (2007).
55. J. Logan, J. S. Fowler, N. D. Volkow, G.-J. Wang, Y.-S. Ding, D. L. Alexoff, Distribution volume ratios without blood sampling from graphical analysis of PET data. *J. Cereb. Blood Flow Metab.* **16**, 834–840 (1996).
56. J. Logan, J. S. Fowler, N. D. Volkow, A. P. Wolf, S. L. Dewey, D. J. Schlyer, R. R. MacGregor, R. Hitzemann, B. Bendriem, S. J. Gatley, D. R. Christman, Graphical analysis of reversible radioligand binding from time—Activity measurements applied to [N-$^{11}$C-methyl]-(–)-cocaine PET studies in human subjects. *J. Cereb. Blood Flow Metab.* **10**, 740–747 (1990).
57. Y. L. Hurd, M. Suzuki, G. C. Sedvall, D1 and D2 dopamine receptor mRNA expression in whole hemisphere sections of the human brain. *J. Chem. Neuroanat.* **22**, 127–137 (2001).
58. A. Abi-Dargham, X. Xu, J. L. Thompson, R. Gil, L. S. Kegeles, N. Urban, R. Narendran, D.-R. Hwang, M. Laruelle, M. Slifstein, Increased prefrontal cortical $D_1$ receptors in drug naïve patients with schizophrenia: A PET study with [$^{11}$C]NNC112. *J. Psychopharmacol.* **26**, 794–805 (2012).

**Acknowledgments:** We thank the study participants. **Funding:** This work was supported by the following funding sources: Howard Hughes Medical Institute (Early Career Physician-Scientist Award) and NIH (K23MH084059, R01MH101425, P41EB015896, S10RR017208, S10RR026666, SR10RR022976, S10RR019933, S10RR023401, R21EB018964, and R01NS083534). This work was conducted with support from Harvard Catalyst, the Harvard Clinical and Translational Science Center (National Center for Research Resources, National Center for Advancing Translational Sciences award UL1TR0011002) and financial contributions from Harvard University and its affiliated academic health care centers. **Author contributions:** J.L.R. obtained funding and principally designed the study; D.N.G., A.A.-D., R.L.B., D.S.M., B.R.R., and J.M.H. contributed to the study design and analysis plan; J.L.R., A.S.T., H.E., N.J.S., N.F.H., A.Z.N., D.B.C., and C.C. obtained data; J.L.R., A.S.T., A.R.-T., D.B.C., and C.C. analyzed the data. All authors contributed to the writing of the manuscript. **Competing interests:** The content is solely the responsibility of the authors and does not necessarily represent the official views of Harvard Catalyst, Harvard University, and its affiliated academic health care centers, or the NIH. The authors declare that they have no competing interests. **Data and materials availability:** All data needed to evaluate the conclusions in the paper are present in the paper and/or the Supplementary Materials. Additional data related to this paper may be requested from the authors.

Submitted 18 November 2015
Accepted 11 May 2016
Published 3 June 2016
10.1126/sciadv.1501672

**Citation:** J. L. Roffman, A. S. Tanner, H. Eryilmaz, A. Rodriguez-Thompson, N. J. Silverstein, N. F. Ho, A. Z. Nitenson, D. B. Chonde, D. N. Greve, A. Abi-Dargham, R. L. Buckner, D. S. Manoach, B. R. Rosen, J. M. Hooker, C. Catana, Dopamine $D_1$ signaling organizes network dynamics underlying working memory. *Sci. Adv.* **2**, e1501672 (2016).

Science Advances

# Dopamine $D_1$ signaling organizes network dynamics underlying working memory

Joshua L. Roffman, Alexandra S. Tanner, Hamdi Eryilmaz, Anais Rodriguez-Thompson, Noah J. Silverstein, New Fei Ho, Adam Z. Nitenson, Daniel B. Chonde, Douglas N. Greve, Anissa Abi-Dargham, Randy L. Buckner, Dara S. Manoach, Bruce R. Rosen, Jacob M. Hooker and Ciprian Catana

*Sci Adv* **2** (6), e1501672.
DOI: 10.1126/sciadv.1501672